

Competing Mechanisms at Vibrated Interfaces of Density-Stratified Fluids

Tianyi Chu,^{1,*} Benjamin Wilfong,¹ Timothy Koehler,² Ryan M. McMullen,² and Spencer H. Bryngelson¹

¹*School of Computational Science & Engineering,
Georgia Institute of Technology, Atlanta, Georgia 30332-0365, USA*

²*Engineering Sciences Center, Sandia National Laboratories,
P.O. Box 5800, Albuquerque, New Mexico 87185-0840, USA*

Fluid–fluid interfacial instability and subsequent fluid mixing are ubiquitous in nature and engineering. Two hydrodynamic instabilities have long been thought to govern the interface behavior: the pressure gradient-driven long-wavelength Rayleigh–Taylor (RT) instability and resonance-induced short-wavelength Faraday instability. However, neither instability alone can explain the dynamics when both mechanisms act concurrently. Instead, we identify a previously unseen multi-modal instability emerging from their coexistence. We show how vibrations govern transitions between the RT and Faraday instabilities, with the two competing instead of resonantly enhancing each other. The initial transient growth is captured by the exponential modal growth of the most unstable Floquet exponent, along with its accompanying periodic behavior. Direct numerical simulations validate these findings and track interface breakup into the multiscale and nonlinear regimes, in which the growing RT modes are shown to suppress Faraday responses via a nonlinear mechanism.

Introduction The interface separating phases in multiphase fluid systems is often subjected to deformation due to internal density differences or external vibrations. These deformations manifest in various forms, including liquid dripping [1–3], bubble injection [4–6], tip streaming [3, 7, 8], and surface waves [9]. Such phenomena are ubiquitous, occurring in natural processes such as rainfall and tidal movements, as well as in engineering applications like atomization and fusion reactions [10, 11]. The unstable growth of these interface deformations eventually leads to interface breakup and fluid mixing. Linear stability analysis predicts two primary hydrodynamic instability mechanisms: the pressure gradient-driven fluid mixing mechanism, triggering the Rayleigh–Taylor (RT) instability [12, 13], and the resonance mechanism, triggering a Faraday instability [14]. Over a century of research has focused on studying these fundamental hydrodynamic instabilities separately, as each is central to a vast range of applications (for RT see [15–20] and for Faraday see [9, 21–26]).

Despite their well-established nature and pervasive observations, a comprehensive understanding of the interface’s behavior when the long-wavelength RT and short-wavelength Faraday instabilities coexist is lacking. This gap is crucial, as vibrations and density stratification often occur simultaneously in realistic situations. Wolf [27, 28] showed via experiment that unstable viscous RT waves can be stabilized *without* generating standing Faraday waves by oscillating the container at specific amplitudes and frequencies. Later studies supported this conclusion through theoretical arguments, and a partial theory was developed [29–33]. However, the coexistence of unstable RT and Faraday modes, where they actively influence

the interface dynamics, has been largely overlooked. The complex interactions and physical mechanisms emerging from this coexistence remain mysterious. This work addresses this gap and provides a comprehensive view of interfacial dynamics under combined density stratification and vibrations.

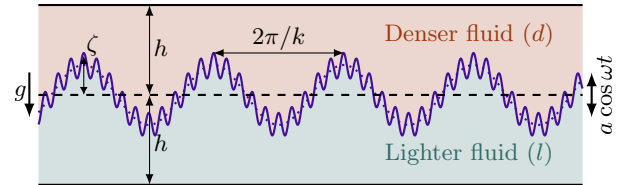


FIG. 1: The two-fluid interface with long-wavelength RT and short-wavelength Faraday instabilities.

We analyze the coexistence and competition of Rayleigh–Taylor (RT) and Faraday instabilities under the effect of external vibrations and internal density differences. We examine the temporal evolution of the interface within the linear regime. Using horizontal homogeneity, we decompose the interface into individual wave numbers, allowing for the investigation of both long-wavelength RT and short-wavelength Faraday waves. Two-dimensional scale-resolved numerical simulations validate the linear theory and capture the system’s evolution into multiscale and nonlinear regimes. We also explore the oscillation–frequency–amplitude phase space to characterize the transition of the dominant instability.

Theoretical Background Consider the interface between two immiscible and incompressible fluids: a denser fluid and a lighter fluid, denoted by subscripts $(\cdot)_d$ and $(\cdot)_l$. The fluids are confined between two

horizontal plates separated by a distance of $2h$ and subject to an oscillatory vertical acceleration

$$\tilde{g}(t) = g^*g + a \cos(\omega t + \varphi_0), \quad (1)$$

where a is the oscillatory amplitude, ω is the corresponding frequency, and φ_0 is the initial phase. Positive gravity, $g^* = 1$, applies when the denser fluid is at the domain bottom, and negative gravity, $g^* = -1$, applies when the denser fluid is on top. [Figure 1](#) shows the two-fluid interface subjected to a harmonic vibration. The time-periodic variation in gravity is suspected to be the driving source of instability, motivating Floquet analysis [34]. We define nondimensionalized quantities, denoted by $(\cdot)^*$, in [table A.1](#) in the End Matter. The temporal evolution of the interface displacement, $\zeta^*(t)$, is decomposed into an exponential term, $e^{\gamma^* t^*}$, that models the growth or decay and a periodic term, $\sum_n \hat{\zeta}_n^* e^{in\omega^* t^*}$, which accounts for the oscillatory fluctuations about it.

We assume that the interface profile is well-defined and single-valued. At each horizontal wavenumber, k^* , a separation into amplitude growth (or decay) and periodic oscillations yields

$$\hat{\zeta}^*(k^*, t^*) = \underbrace{e^{\gamma^* t^*}}_{\text{Modal}} \underbrace{\sum_{n=-\infty}^{\infty} \hat{\zeta}_n^*(k^*) e^{in\omega^*(t^*+t_0^*)}}_{\text{Periodic components}}, \quad (2)$$

where γ^* is the Floquet exponent, t_0^* is the time shift associated with the initial phase φ_0 , and n is the index of the harmonics [23, 24]. A positive real Floquet exponent indicates instability, driving the system toward interface breakup. Floquet exponents, often obtained through the eigenvalue decomposition of the monodromy matrix, are not unique and collectively describe nonmodal growth. Here, we demonstrate that the modal growth of the most unstable Floquet exponent, γ_U^* , combined with the periodic components, accurately predicts the initial transient dynamics. By relating the interface displacements at different orders of harmonics, γ_U^* is found for each wavenumber by solving

$$\gamma_U^* = \underset{\det\{\mathbf{A}(\gamma^*; k^*) - a^* \mathbf{B}\}=0}{\operatorname{argmax}} \operatorname{Re}\{\gamma^*\}. \quad (3)$$

The periodic components at different harmonics, $\hat{\zeta}^*$, can be then found as the null space of $(\mathbf{A} - a^* \mathbf{B})$. A detailed analysis is provided in the End Matter. Equation (3) shows a generalized analysis of the hydrodynamic instability in fluid mixing, covering a wide range of configuration parameters, including viscosity, surface tension, vibration, and density dif-

ferences. In the static limit ($a^* \rightarrow 0$), Eq. (3) becomes

$$\gamma_U^* = \underset{A_0(\gamma^*; k^*)=0}{\operatorname{argmax}} \operatorname{Re}\{\gamma^*\}, \quad (4)$$

as only $n = 0$ survives the simplification of Eq. (2). This form recovers the classical RT dispersion relation [35]. The critical acceleration, a_c^* , for neutral stability is obtained by constraining the displacement in Eq. (3) to exhibit pure sinusoidal harmonic (H), $\gamma_U^* = 0$, or subharmonic (S), $\gamma_U^* = i\omega^*/2$, responses, which recovers the generalized eigenvalue problem,

$$\mathbf{A}(\gamma_U^* = 0 \text{ or } i\omega^*/2; k^*) \hat{\zeta}^* = a_c^* \mathbf{B} \hat{\zeta}^*, \quad (5)$$

for the Faraday instability [23, 24]. Beyond the identification of the stability boundary, Eq. (2) enables the prediction of transient wave dynamics at a given wavenumber k^* within the unstable regime. Together, these analyses enable the dissection of the mechanics as the system transitions toward nonlinear interface breakup. An example of this utility is shown next.

Results For demonstration purposes, we consider polydimethylsiloxane (PDMS) as the more dense fluid, characterized by a density of $\rho_d = 950 \text{ kg/m}^3$, kinematic viscosity of $\nu_d = 2 \times 10^{-5} \text{ m}^2/\text{s}$, and surface tension coefficient of $\sigma_d = 2.06 \times 10^{-2} \text{ N/m}$. The gravitational acceleration is set to $g = 9.81 \text{ m/s}^2$. The properties of the lighter fluid are determined by the density and viscosity ratios, At and η , respectively. To validate the linear theory predictions, we perform high-fidelity 2D simulations using MFC [36], a GPU-accelerated compressible multiphase flow solver [37, 38]. The multiphase system is governed by the six-equation diffuse interface model [39] with surface tension [40], solved via a high-order finite-volume method and temporal discretizations with closure by the stiffened gas equation of state. Specific heat ratios and liquid stiffness parameters are selected to match the fluid internal energy and speed of sound at rest. Additional details on nondimensionalization and simulation setup are provided in the End Matter. [Table I](#) summarizes the configurations studied.

TABLE I: Configurations studied.

Cases	h [mm]	a^*	g^*	ω^*	(At, η)	k^*	γ_U^* (S/H)
Figure 3 (b)	13.00	16	-1	33.9	(0.9,0.1)	2.89	1.21 (H)
	13.00	16	-1	33.9	(0.9,0.1)	29.1	1.21 (S)
Figure 3 (c)	13.00	18	-1	27.4	(0.9,0.1)	2.04	0.96 (H)
	13.00	18	-1	27.4	(0.9,0.1)	24.5	3.45 (S)
Figure 4 (b)	26.87	10	1	24.6	(1,0)	31.4	3.77 (S)
Figure 4 (c)	21.81	15	1	29.6	(1,0)	31.4	4.47 (S)
Figure 4 (d)	16.75	30	1	39.0	(1,0)	31.4	6.80 (S)
Figure 4 (e)	12.95	30	1	45.7	(1,0)	31.4	3.61 (S)

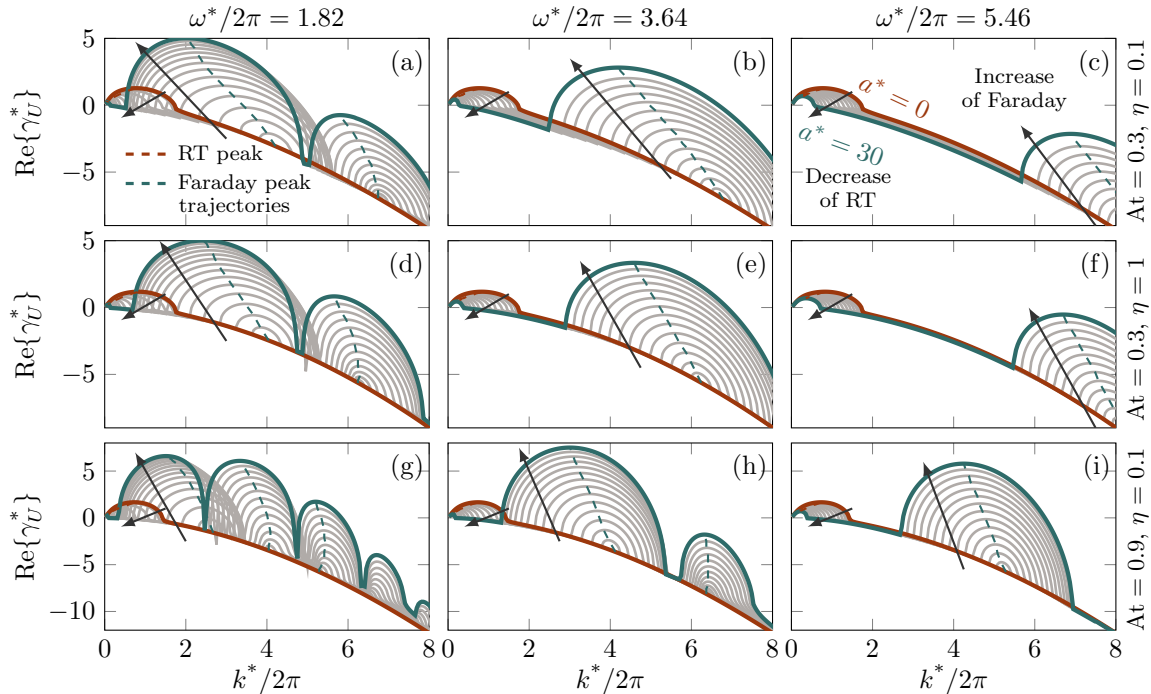


FIG. 2: Interface displacement growth rate for $g^* = -1$ under various parameter combinations, with arrows denoting the transition from $a^* = 0$ to $a^* = 30$.

We focus on the case where both the RT and Faraday instabilities coexist, achieved by considering a negative gravity ($g^* = -1$). Figure 2 shows the growth rates of the displacement of the interface for various combinations of parameters. The lighter fluid properties are chosen to approximate three types of interfaces: inviscid liquid–liquid ($At = 0.3$, $\eta = 0.1$), liquid–liquid ($At = 0.3$, $\eta = 1$), and gas–liquid ($At = 0.9$, $\eta = 0.1$). In the absence of vibration, $a^* = 0$, classical RT instability manifests as a low-wavenumber peak. As the oscillation amplitude increases, the amplitude of the positive peak diminishes toward zero, while its position shifts toward the origin. Within a finite horizontal domain, this leads to the truncation of the RTs wave with $k^* \rightarrow 0$. This behavior demonstrates the theoretical principle of dynamic stabilization of RT waves under vibration [27, 28]. Given its continuous evolution with increasing vibration, we refer to the instability mechanism of the low-wavenumber peak as RT-type. The Floquet exponent associated with the RT peak is purely real and can thus be generalized to the cases of harmonic response. The Faraday instability emerges as the vibration amplitude increases, marked by a distinct peak at higher wavenumbers that shifts downward. The increasing prominence of the Faraday peak does not resonate with the RT

peak. Instead, the RT peak is suppressed and pushed towards the zero-wavenumber limit, further highlighting the competitive interplay between these two phenomena. For all oscillating frequencies considered, the boundary layer thickness, $\delta \equiv \sqrt{2\nu_d/\omega}$, remains much lower than the fluid depth, with a maximum ratio of $\delta/h \leq 0.027$. In this regime, the onset of the Faraday instability is subharmonic [24]. While an increase in the viscosity ratio, η , has little effect on the growth rate profiles, increasing the density ratio, At , induces local peaks at higher harmonics. Unstable higher-order harmonics occur at the lowest oscillation frequency ($\omega^*/2\pi = 1.82$) in fig. 2 (d, g), complementing the dominant Faraday subharmonic mode. As expected, increasing the oscillation magnitude will eventually cause the Faraday peak to surpass the RT peak. This transition between the two fundamental hydrodynamic instabilities leads to a mixed region where *both instabilities coexist*, potentially altering the dynamics of the interface.

Figure 3 (a) shows the dominant growth rate within the oscillating frequency–amplitude phase space. The transition of the leading instability mechanism from RT to Faraday can be observed in three stages. At low oscillation amplitudes, the RT instability is the dominant phenomenon. For larger oscillation amplitudes, the Faraday instability approaches its unstable

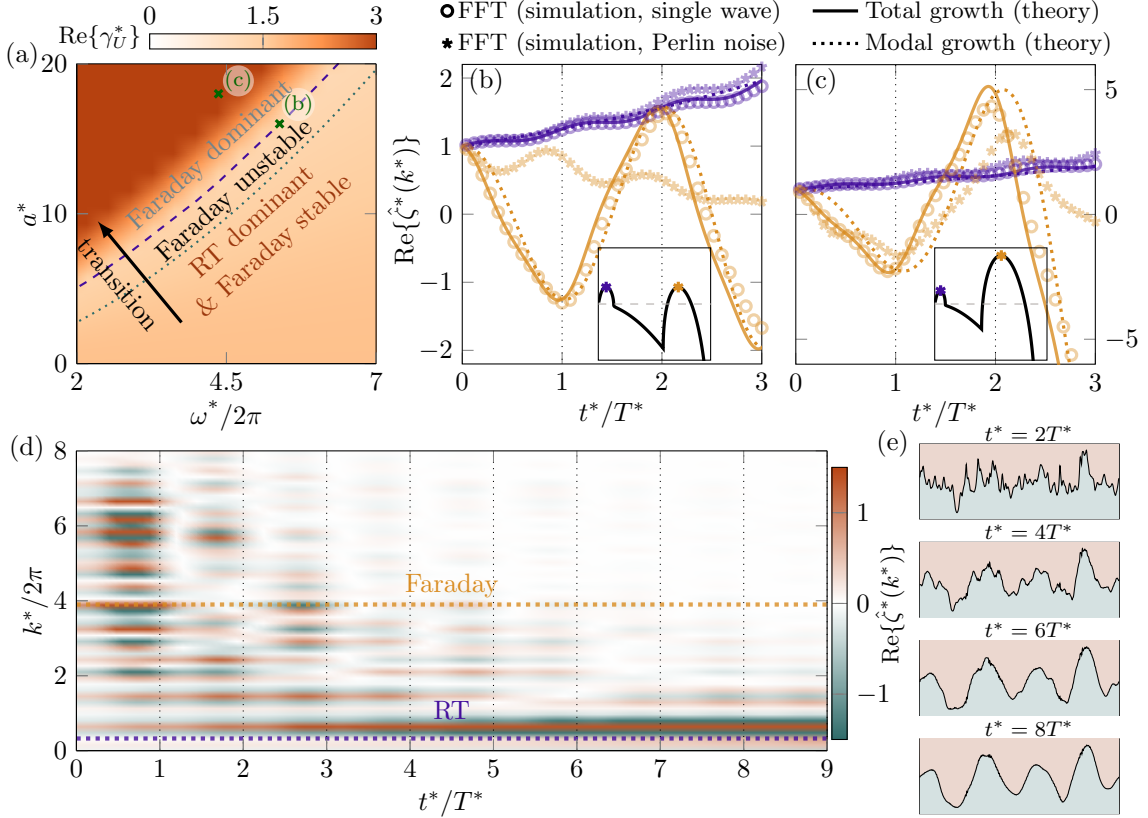


FIG. 3: Multi-modal instability analysis for $(At, \eta) = (0.9, 0.1)$: (a) dominant growth rate in the oscillating frequency-amplitude phase space, with the margins for the Faraday stability and the RT-Faraday transition highlighted; (b,c) normalized Faraday and RT wave evolutions with growth rates (insets) for cases marked by green crosses in (a), under single-mode or Perlin noise excitations. The wavenumber–time diagram (d) and not-to-scale interface profiles (e) show the nonlinear damping of Faraday waves for the Perlin noise case in (c).

boundary, yet the RT mechanism is dominant. Finally, at sufficiently high oscillation amplitudes, the growth rate of the Faraday instability surpasses that of the RT instability. For a given oscillation frequency, the thresholds of these two stages differ by about $2a^*$.

To quantitatively compare theoretical predictions and numerical simulations, we perturb the initial interface with three profiles: single-mode RT and Faraday sine waves and multiscale Perlin noise perturbations [41]. The temporal dynamics of the normalized RT and Faraday modes are shown in fig. 3 (b, c), corresponding to the two cases marked in fig. 3 (a). While classical linear stability analysis of the static RT problem predicts purely exponential modal growth, the presence of vibrations induces an oscillatory pattern around this baseline growth. Owing to its subharmonic nature, the Faraday displacement becomes negative at $t^* = T^*$. The interface rebounds to a positive peak that either intersects the RT displacement (panel b) or exceeds it (panel c) at $t^* = 2T^*$, where

$T^* \equiv 2\pi/\omega^*$. For perturbations with a single sine wave, the modal growth of the most unstable Floquet exponent, $e^{\gamma v^* t^*}$, exhibits favorable agreement with the Fourier components obtained from simulations at integer multiples of the oscillation period. This alignment confirms that the interface growth follows Floquet theory. By incorporating the modal growth with the additional periodic terms, the total growth defined in Eq. (2) accurately predicts the interface dynamics during the first oscillation period, even with a broadband initial wavenumber spectrum. Beyond this period, the theory remains in qualitative agreement with simulations, although minor deviations arise due to nonlinear effects. Simulations initialized with Perlin noise exhibit suppressed growth rates and reduced amplitudes of Faraday waves compared to theoretical predictions. In the absence of competing wavelengths, these waves would exhibit Floquet-type growth and ultimately induce interface breakup, suggesting that

the observed suppression is primarily attributable to nonlinear damping effects. When the Faraday growth rate exceeds that of RT, the theory remains qualitatively predictive of the system’s dynamics, despite the presence of multiscale waves. In contrast, the growth of RT waves is generally unaffected.

To illustrate transient interface dynamics across wavenumbers in a realistic context, [fig. 3\(d\)](#) presents the wavenumber–time diagram for the Perlin noise case shown in [fig. 3\(c\)](#). This case exemplifies the nonlinear damping of Faraday waves despite a dominant linear growth rate. The coexistence of RT and Faraday waves is clearly observed within the given time window. Wavenumbers near the Faraday peak exhibit periodic phase changes due to their dominance of the subharmonic nature, whereas those near the RT peak display steady growth. The insets of [fig. 3 \(d\)](#) show the resulting interface profiles and highlight the competition between steadily amplifying long-wavelength RT waves and oscillatory short-wavelength Faraday waves. Initially ($t \lesssim 2.5T^*$), the interface profile is dominated by Faraday waves due to their higher initial growth rate. As time progresses, long-wavelength RT waves amplify and prevail, though residual small-scale Faraday oscillations persist. This transition implies that the growing low-wavenumber RT components nonlinearly dampen the high-wavenumber subharmonic Faraday responses, despite the inherent instability of these latter responses. As shown in [fig. 3 \(b, c\)](#), the Faraday waves would otherwise grow unimpeded toward interface breakup in the absence of RT competition. The dominance of RT waves suppresses this pathway, redirecting the system toward RT-driven dynamics. This mechanism has been verified by exciting the interface using only the linear superposition of Faraday and RT waves (not shown). Together, these results demonstrate the nonlinear transient dynamics that govern fluid interfaces under the combined effects of density and vibration.

Conclusion This letter presents a theoretical and computational investigation into the previously unexplored coexistence and competition of two fundamental hydrodynamic instabilities: the pressure gradient-driven Rayleigh–Taylor (RT) instability and the resonance-induced Faraday instability. Through linear Floquet stability analysis and 2D numerical simulations, we demonstrate that interface growth under combined density and vibration effects exhibits a Floquet-type behavior: total displacement decomposes into modal growth of the most unstable Floquet mode and harmonic oscillations from periodic terms. Our key finding is the discovery of a novel multimodal instability region, where the RT and Faraday

instabilities coexist and compete in non-trivial ways. This region emerges as the oscillation magnitude increases, marking a gradual transition in the dominant instability mechanism from RT to Faraday. Within this region, we observed a unique competitive interaction: the Faraday instability consistently suppresses the RT instability toward the zero-wavenumber limit, while the residual RT mechanism, in turn, attenuates the Faraday responses via a nonlinear damping mechanism, even when the initial growth rate of the Faraday instability exceeds that of RT. Furthermore, the coexistence of these mechanisms generates multiscale interfacial waves, culminating in interfacial breakup phenomena that are ubiquitous in both natural and engineered systems, yet remain uncharted in prior studies.

The discovery of the coexistence and competition between RT and Faraday instabilities offers new insights into predicting and controlling fluid interfaces in vibration-prone systems. Our findings bridge fundamental hydrodynamics and engineering, leveraging instability interactions of the fluid to control the interface kinematics. Vibrations dynamically stabilize RT modes while exciting Faraday instabilities, and the inclusion of RT waves, in turn, nonlinearly dampens the unstable Faraday response. By tuning the oscillation, processes such as atomization or inertial confinement fusion can be optimized to suppress both low- and high-wavenumber instabilities, thereby enhancing efficiency and preventing failure. These insights also open up new avenues for studying transient dynamics in both natural and engineered fluid systems, where external vibrations compete with intrinsic instabilities, ranging from geophysical flows to the injection of bubbles.

Acknowledgments Sandia National Laboratories is a multi-mission laboratory managed and operated by National Technology & Engineering Solutions of Sandia, LLC (NTESS), a wholly owned subsidiary of Honeywell International Inc., for the U.S. Department of Energy’s National Nuclear Security Administration (DOE/NNSA) under contract DE-NA0003525. This written work is authored by an employee of NTESS. The employee, not NTESS, owns the right, title and interest in and to the written work and is responsible for its contents. Any subjective views or opinions that might be expressed in the written work do not necessarily represent the views of the U.S. Government. The publisher acknowledges that the U.S. Government retains a nonexclusive, paid-up, irrevocable, world-wide license to publish or reproduce the published form of this written work or allow others to do so, for U.S. Government purposes.

The DOE will provide public access to results of federally sponsored research in accordance with the [DOE Public Access Plan](#). This work used the resources of the Oak Ridge Leadership Computing Facility at the Oak Ridge National Laboratory, which is supported by the Office of Science of the U.S. Department of Energy under Contract No. DE-AC05-00OR22725 (PI Bryngelson, allocation CFD154). This work also used Bridges2 at the Pittsburgh Supercomputing Center through allocation TG-PHY210084 (PI Spencer Bryngelson) from the Advanced Cyberinfrastructure Coordination Ecosystem: Services & Support (ACCESS) program, which is supported by National Science Foundation grants #2138259, #2138286, #2138307, #2137603, and #2138296. The authors thank F. Pierce and J. S. Horner for helpful discussions about this work.

Data availability Code available at <https://github.com/MFlowCode/MFC>.

-
- * **Contact author:** tchu72@gatech.edu
- [1] S. Wilson, The slow dripping of a viscous fluid, *J. Fluid Mech.* **190**, 561 (1988).
 - [2] C. Clanet and J. C. Lasheras, Transition from dripping to jetting, *J. Fluid Mech.* **383**, 307 (1999).
 - [3] J. M. Montanero and A. M. Gañán-Calvo, Dripping, jetting and tip streaming, *Rep. Prog. Phys.* **83**, 097001 (2020).
 - [4] H. H. Bleich, Effect of vibrations on the motion of small gas bubbles in a liquid, *J. Jet Propuls.* **26**, 958 (1956).
 - [5] K. Chen and H. J. Richter, Instability analysis of the transition from bubbling to jetting in a gas injected into a liquid, *Int. J. Multiph. Flow* **23**, 699 (1997).
 - [6] G. Yang, B. Du, and L. Fan, Bubble formation and dynamics in gas–liquid–solid fluidization—a review, *Chem. Eng. Sci.* **62**, 2 (2007).
 - [7] C. D. Eggleton, T.-M. Tsai, and K. J. Stebe, Tip streaming from a drop in the presence of surfactants, *Phys. Rev. Lett.* **87**, 048302 (2001).
 - [8] R. T. Collins, J. J. Jones, M. T. Harris, and O. A. Basaran, Electrohydrodynamic tip streaming and emission of charged drops from liquid cones, *Nat. Phys.* **4**, 149 (2008).
 - [9] J. Miles and D. Henderson, Parametrically forced surface waves, *Annu. Rev. Fluid Mech.* **22**, 143 (1990).
 - [10] R. S. Craxton, K. S. Anderson, T. R. Boehly, V. N. Goncharov, D. R. Harding, J. P. Knauer, R. L. McCrory, P. W. McKenty, D. D. Meyerhofer, J. F. Myatt, *et al.*, Direct-drive inertial confinement fusion: A review, *Phys. Plasmas* **22** (2015).
 - [11] R. Betti and O. A. Hurricane, Inertial-confinement fusion with lasers, *Nat. Phys.* **12**, 435 (2016).
 - [12] R. L., Investigation of the character of the equilibrium of an incompressible heavy fluid of variable density, *Proc. London Math. Soc.* **1**, 170 (1882).
 - [13] G. I. Taylor, The instability of liquid surfaces when accelerated in a direction perpendicular to their planes. i, *Phil. Trans. R. Soc. A* **201**, 192 (1950).
 - [14] M. Faraday, Xvii. On a peculiar class of acoustical figures; and on certain forms assumed by groups of particles upon vibrating elastic surfaces, *Phil. Trans. R. Soc.* , 299 (1831).
 - [15] W. J. Harrison, The influence of viscosity on the oscillations of superposed fluids, *Proc. London Math. Soc.* **2**, 396 (1908).
 - [16] R. Bellman and R. H. Pennington, Effects of surface tension and viscosity on Taylor instability, *Q. Appl. Math.* **12**, 151 (1954).
 - [17] M. S. Plesset and C. G. Whipple, Viscous effects in Rayleigh–Taylor instability, *Phys. Fluids* **17**, 1 (1974).
 - [18] D. H. Sharp, *Overview of Rayleigh–Taylor instability*, Tech. Rep. (Los Alamos National Laboratory (LANL), 1983).
 - [19] H.-J. Kull, Theory of the Rayleigh–Taylor instability, *Phys. Rep.* **206**, 197 (1991).
 - [20] A. R. Piriz, O. D. Cortázar, J. J. López Cela, and N. A. Tahir, The Rayleigh–Taylor instability, *Am. J. Phys.* **74**, 1095 (2006).
 - [21] T. B. Benjamin and F. J. Ursell, The stability of the plane free surface of a liquid in vertical periodic motion, *Phil. Trans. R. Soc. A* **225**, 505 (1954).
 - [22] S. Fauve, K. Kumar, C. Laroche, D. Beysens, and Y. Garrabos, Parametric instability of a liquid-vapor interface close to the critical point, *Phys. Rev. Lett.* **68**, 3160 (1992).
 - [23] K. Kumar and L. S. Tuckerman, Parametric instability of the interface between two fluids, *J. Fluid Mech.* **279**, 49 (1994).
 - [24] K. Kumar, Linear theory of faraday instability in viscous liquids, *Proc. R. Soc. Lond. A* **452**, 1113 (1996).
 - [25] J. Wright, S. Yon, and C. Pozrikidis, Numerical studies of two-dimensional Faraday oscillations of inviscid fluids, *J. Fluid Mech.* **402**, 1 (2000).
 - [26] S. Kumar, Mechanism for the Faraday instability in viscous liquids, *Phys. Rev. E* **62**, 1416 (2000).
 - [27] G. H. Wolf, The dynamic stabilization of the Rayleigh–Taylor instability and the corresponding dynamic equilibrium, *Z. Physik* **227**, 291 (1969).
 - [28] G. H. Wolf, Dynamic stabilization of the interchange instability of a liquid-gas interface, *Phys. Rev. Lett.* **24**, 444 (1970).
 - [29] F. Troyon and R. Gruber, Theory of the dynamic stabilization of the Rayleigh–Taylor instability, *Phys. Fluids* **14**, 2069 (1971).
 - [30] V. Lapuerta, F. J. Mancebo, and J. M. Vega, Control of Rayleigh–Taylor instability by vertical vibration in large aspect ratio containers, *Phys. Rev. E* **64**, 016318 (2001).
 - [31] A. R. Piriz, G. Rodriguez P., I. Munoz D., J. J. Lopez C., and N. A. Tahir, Dynamic stabilization of Rayleigh–Taylor instability in Newtonian fluids, *Phys. Rev. E* **82**, 026317 (2010).
 - [32] E. Serman-Cohen, M. Bestehorn, and A. Oron, Rayleigh–Taylor instability in thin liquid films sub-

- jected to harmonic vibration, *Phys. Fluids* **29** (2017).
- [33] A. Pototsky and M. Bestehorn, Faraday instability of a two-layer liquid film with a free upper surface, *Phys. Rev. Fluids* **1**, 023901 (2016).
- [34] G. Floquet, Sur les équations différentielles linéaires à coefficients périodiques, in *Ann. Sci. Ecole. Norm. S.*, Vol. 12 (1883) pp. 47–88.
- [35] S. Chandrasekhar, *Hydrodynamic and Hydromagnetic Stability* (Oxford University Press, 1961).
- [36] S. H. Bryngelson, K. Schmidmayer, V. Coralic, J. C. Meng, K. Maeda, and T. Colonius, MFC: An open-source high-order multi-component, multi-phase, and multi-scale compressible flow solver, *Comp. Phys. Comm.* **266**, 107396 (2021).
- [37] A. Radhakrishnan, H. Le Berre, B. Wilfong, J.-S. Spratt, M. Rodriguez Jr., T. Colonius, and S. H. Bryngelson, Method for portable, scalable, and performant GPU-accelerated simulation of multiphase compressible flow, *Comput. Phys. Commun.* **302**, 109238 (2024).
- [38] B. Wilfong, H. Le Berre, A. Radhakrishnan, A. Gupta, D. Vaca-Revelo, D. Adam, H. Yu, H. Lee, J. R. Chreim, M. Carcana Barbosa, Y. Zhang, E. Cisneros-Garibay, A. Gnanaskandan, M. Rodriguez Jr., R. D. Budiardja, S. Abbott, T. Colonius, and S. H. Bryngelson, MFC 5.0: An exascale many-physics flow solver, arXiv:2503.07953 (2025).
- [39] R. Saurel, F. Petitpas, and R. Abgrall, Modelling phase transition in metastable liquids: application to cavitating and flashing flows, *J. Fluid Mech.* **607**, 313–350 (2008).
- [40] K. Schmidmayer, F. Petitpas, E. Daniel, N. Favrie, and S. Gavriluk, A model and numerical method for compressible flows with capillary effects, *J. Comput. Phys.* **334**, 468 (2017).
- [41] K. Perlin, Improving noise, *ACM Trans. Graph.* **21**, 681–682 (2002).

End Matter

Linear Floquet stability analysis Consider two immiscible fluids, each with horizontal homogeneity and a depth h , separated by an interface. Within each fluid layer j , the motion of the fluid is governed by the incompressible Navier–Stokes equations,

$$\rho_j [\partial_t + (\mathbf{u}_j \cdot \nabla)] \mathbf{u}_j = -\nabla p_j - \rho_j \tilde{g} \mathbf{e}_z + \mu_j \nabla^2 \mathbf{u}_j, \quad (\text{A.1a})$$

$$\nabla \cdot \mathbf{u}_j = 0, \quad (\text{A.1b})$$

where $\tilde{g}(t) = g^* g + a \cos(\omega t)$ is the temporally modulated gravitational acceleration. We can decompose the flow state around the equilibrium-state solution of the Navier–Stokes equations (A.1) as $\mathbf{u}_j = \mathbf{U}_j + \mathbf{u}'_j$, $p_j = P_j + p'_j$, where $(\mathbf{U}_j, P_j) = (0, -\rho_j \tilde{g} \mathbf{e}_z)$ and $(\cdot)'$ denotes the small fluctuating components. The governing equations for the fluctuations are

$$\rho_j \partial_t \mathbf{u}'_j = -\nabla p'_j + \mu_j \nabla^2 \mathbf{u}'_j, \quad \nabla \cdot \mathbf{u}'_j = 0. \quad (\text{A.2})$$

Applying the operator $\mathbf{e}_z \cdot \nabla \times \nabla \times$ to (A.2) eliminates the horizontal velocity components, resulting in

$$(\partial_t - \nu_j \nabla^2) \nabla^2 w'_j = 0. \quad (\text{A.3})$$

We expand the horizontal velocity and interface displacement in the horizontal plane using a Fourier series, and we introduce a Floquet expansion to account for periodic temporal growth. This yields

$$\begin{aligned} & [w'_j(k, z, t), \zeta(k, t)] \\ &= e^{\gamma t + ikx} \sum_{n=-\infty}^{\infty} [\hat{w}_{n,j}(k, z), \hat{\zeta}_{n,j}(k)] e^{in\omega t}, \end{aligned} \quad (\text{A.4})$$

Substituting (A.4) into (A.3) gives

$$[\gamma_n - \nu_j (\partial_{zz} - k^2)] (\partial_{zz} - k^2) \hat{w}_{n,j} = 0, \quad (\text{A.5})$$

and the general solution of this dispersion relation is $\hat{w}_{n,j} = a_{n,j} e^{kz} + b_{n,j} e^{-kz} + c_{n,j} e^{q_{n,j} z} + d_{n,j} e^{-q_{n,j} z}$, where $\gamma_n \equiv \gamma + in\omega$ and $q_{n,j} \equiv \sqrt{k^2 + (\gamma + in\omega)/\nu_j}$. No-slip boundary conditions at the two plates yield $\hat{w}_{n,h} = \partial_z \hat{w}_{n,h} = 0$ at $z = -h$, and $\hat{w}_{n,l} = \partial_z \hat{w}_{n,l} = 0$ at $z = h$. At the interface $z = \zeta$, the continuity of velocity and tangential stress and the kinematic boundary condition yield

$$\hat{w}_{n,l} = \hat{w}_{n,h}, \quad (\text{A.6})$$

$$\partial_z \hat{w}_{n,l} = \partial_z \hat{w}_{n,h}, \quad (\text{A.7})$$

$$\mu_l (\partial_{zz} + k^2) \hat{w}_{n,l} = \mu_d (\partial_{zz} + k^2) \hat{w}_{n,h}, \quad (\text{A.8})$$

$$\gamma_n \hat{\zeta}_n = \hat{w}_n|_{z=0}. \quad (\text{A.9})$$

Substituting the general solutions of $\hat{w}_{n,j}$ into the above 8-equation boundary condition, we find $\mathbf{Q}_n(a_{n,h}, b_{n,h}, c_{n,h}, d_{n,h}, a_{n,l}, b_{n,l}, c_{n,l}, d_{n,l})^\top = (\gamma_n \hat{\zeta}_n, 0, 0, 0, 0, 0, 0, 0)^\top$. Upon nondimensionalization using table A.1 and further simplification, the matrix \mathbf{Q}_n can be written as (A.11). Here, the superscripts $(\cdot)^+$ and $(\cdot)^-$ are used to denote $q^+ \equiv q + 1$ and $q^- \equiv q - 1$. When the depth $h \rightarrow \infty$, the vanishing velocity gives $b_{n,h} = d_{n,h} = a_{n,l} = c_{n,l} = 0$.

TABLE A.1: Dimensionless quantities.

Dimensionless quantity	Quantity name
$t_c = \sqrt{h/g}$	Gravitational time
$\text{At} = (\rho_d - \rho_l)/(\rho_d + \rho_l)$	Atwood number
$\eta = \mu_l/\mu_d$	Viscosity ratio
$C = \nu_d/(gh^3)$	Viscous-to-gravitational force ratio
$\text{Bd} = \rho_d gh^2/\sigma_d$	Bond number
$a^* = a/g$	Acceleration
$\zeta^* = \zeta/h$	Interface displacement
$k^* = kh$	Wavenumber
$t^* = t/t_c$	Time
$\gamma^* = \gamma t_c$	Growth rate
$\omega^* = \omega t_c$	Oscillatory frequency

The jump condition for pressure at the interface is

$$\begin{aligned} & [\delta\rho\gamma_n - \delta\mu\partial_{zz} + 3\delta\mu k^2] \partial_z \hat{w}_n + (\delta\rho g^* g k^2 - \sigma k^2) \hat{\zeta}_n \\ &= \frac{1}{2} \delta\rho k^2 a (\hat{\zeta}_n + \hat{\zeta}_{n+1}), \end{aligned} \quad (\text{A.10})$$

where δ represents the jump across the interface. Relating different orders of harmonics, $\hat{\zeta}_n^*$, in (A.10) results in the linear system shown in (A.12) to (A.13). In practice, (A.12) is truncated at $n = 10$, resulting in a 22×22 linear problem. The Floquet exponents γ^* are found by solving $\det\{\mathbf{A}(\gamma^*; k^*) - a^* \mathbf{B}\} = 0$. The oscillations at each order of harmonics, $\hat{\zeta}_n^*$, spans the null space of $(\mathbf{A} - a^* \mathbf{B})$. Together, they predict the linear transient growth of the interface.

MFC simulations The computational domain spans four wavelengths of interest in width, with each fluid layer having a depth of $h = 0.013$ m. A uniform Cartesian mesh resolves the shortest wavelength with 192 cells, as validated by a convergence study. Periodic and no-slip boundary conditions are applied at the horizontal and vertical boundaries. The interface is initially perturbed by a height that is 1% of the wavelength, and hydrodynamic equilibrium is achieved at the interface with a pressure of 100 kPa.

We verify the linear theory predictions for the RT stable case, where $g^* = 1$. A startup period lasting a

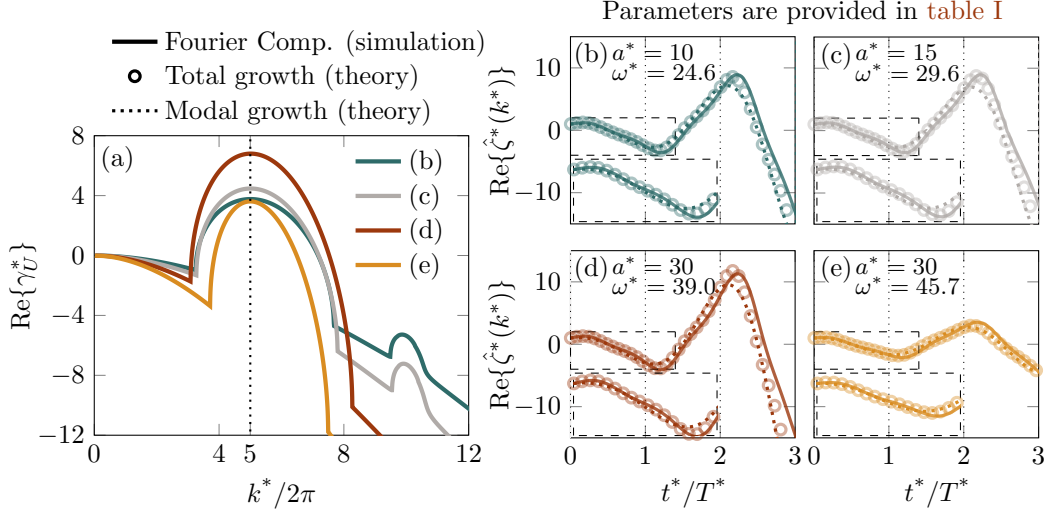


FIG. 4: Analysis of cases with the most unstable wavenumber $k^*/2\pi = 5$ for $g^* = 1$: (a) Growth rates; (b–e) Temporal evolution of the most unstable waves, with a zoomed-in view capturing the first period.

quarter of an oscillation cycle initiates fluid motion, ensuring consistency with the non-zero velocity fields predicted by linear theory. [Figure 4](#) (a) shows the growth rates for four cases; see [table I](#). The temporal evolution of the interface displacements for the most unstable waves, $k^*/2\pi = 5$, over three oscillation

periods is shown in [fig. 4](#) (b–e). Akin to [fig. 3](#) (b, c), initial transient dynamics of the Faraday waves are captured by the exponential modal growth of the most unstable Floquet exponent and its associated periodic behavior. These Faraday waves grow subharmonically and eventually lead to interface breakup.

$$\mathbf{Q}_n^* \equiv \begin{pmatrix} 1 & 1 & 1 & 1 & 0 & 0 & 0 & 0 \\ 1 & 1 & 1 & 1 & -1 & -1 & -1 & -1 \\ 1 & -1 & q_{n,h} & -q_{n,h} & -1 & 1 & -q_{n,l} & q_{n,l} \\ 2 & 2 & 1 + q_{n,h}^2 & 1 + q_{n,h}^2 & -2\eta & -2\eta & -\eta(1 + q_{n,l}^2) & -\eta(1 + q_{n,l}^2) \\ e^{-k^* q_{n,h}^+} & e^{-k^* q_{n,h}^-} & e^{-2k^* q_{n,h}^+} & 1 & 0 & 0 & 0 & 0 \\ q_{n,h}^+ e^{-2k^*} & -q_{n,h}^- & 2q_{n,h} e^{-k^* q_{n,h}^+} & 0 & 0 & 0 & 0 & 0 \\ 0 & 0 & 0 & 0 & e^{-k^* q_{n,l}^-} & e^{-k^* q_{n,l}^+} & 1 & e^{-2k^* q_{n,l}} \\ 0 & 0 & 0 & 0 & -q_{n,l}^- & q_{n,l}^+ e^{-2k^*} & 0 & 2e^{-k^* q_{n,l}^+} \end{pmatrix}. \quad (\text{A.11})$$

$$\left[\underbrace{\begin{pmatrix} \ddots & \vdots & \vdots & \vdots & \vdots \\ \cdots & A_{-1} & 0 & 0 & \cdots \\ \cdots & 0 & A_0 & 0 & \cdots \\ \cdots & 0 & 0 & A_1 & \cdots \\ \vdots & \vdots & \vdots & \vdots & \ddots \end{pmatrix}}_A - a^* \underbrace{\begin{pmatrix} \ddots & \vdots & \vdots & \vdots & \vdots \\ \cdots & 0 & 1 & 0 & \cdots \\ \cdots & 1 & 0 & 1 & \cdots \\ \cdots & 0 & 1 & 0 & \cdots \\ \vdots & \vdots & \vdots & \vdots & \ddots \end{pmatrix}}_B \right] \underbrace{\begin{pmatrix} \vdots \\ \hat{\zeta}_{-1}^* \\ \hat{\zeta}_0^* \\ \hat{\zeta}_1^* \\ \vdots \end{pmatrix}}_{\hat{\zeta}^*} = 0, \quad \text{where} \quad (\text{A.12})$$

$$A_n(\gamma^*; k^*) \equiv -2Ck^*(1 + At)/(2At) (a_{n,h} - b_{n,h} + c_{n,h}q_{n,h}^{*3} - d_{n,h}q_{n,h}^{*3}) + 2(g^* + k^{*2}(1 + At)/(2Bd)) \\ + 2k^* (a_{n,h} - b_{n,h} + c_{n,h}q_{n,h}^* - d_{n,h}q_{n,h}^*) \left(\gamma_n^*/(Ck^{*2}) + 3C(1 - \eta)(1 + At)/(2At) \right). \quad (\text{A.13})$$